ISSN 1674-1056
http://cpb.iphy.ac.cn
http://iopscience.iop.org/cpb
中国物理 B
Chinese Physics
中国物理 Chinese Physics B

Current improvement in substrate structured Sb_2S_3 solar cells with $MoSe_2$ interlayer

Lu Liu(刘璐), Sheng-Li Zhang(张生利), Jian-Yu Wu(吴建宇), Wei-Huang Wang(王伟煌), Wei Liu(刘玮), Li Wu(武莉), Yi Zhang(张毅)

Citation: Chin. Phys. B . 2020, 29(5): 058801 . **doi:** 10.1088/1674-1056/ab8220
Journal homepage: http://cpb.iphy.ac.cn; http://iopscience.iop.org/cpb

What follows is a list of articles you may be interested in

Two-step processed efficient perovskite solar cells via improving perovskite/PTAA interface using solvent engineering in PbI_2 precursor

Cao-Yu Long(龙操玉), Ning Wang(王宁), Ke-Qing Huang(黄可卿), Heng-Yue Li(李恒月), Biao Liu(刘标), Jun-Liang Yang(阳军亮)

Chin. Phys. B . 2020, 29(4): 048801 . **doi:** 10.1088/1674-1056/ab7744

Microstructure evolution and passivation quality of hydrogenated amorphous silicon oxide ($a\text{-}SiO_x$:H) on <100>- and <111>-orientated c-Si wafers

Jun-Fan Chen(陈俊帆), Sheng-Sheng Zhao(赵生盛), Ling-Ling Yan(延玲玲), Hui-Zhi Ren(任慧志), Can Han(韩灿), De-Kun Zhang(张德坤), Chang-Chun Wei(魏长春), Guang-Cai Wang(王广才), Guo-Fu Hou(侯国付), Ying Zhao(赵颖), Xiao-Dan Zhang(张晓丹)

Chin. Phys. B . 2020, 29(3): 038801 . **doi:** 10.1088/1674-1056/ab6c47

Designing solar-cell absorber materials through computational high-throughput screening

Xiaowei Jiang(江小蔚), Wan-Jian Yin(尹万健)

Chin. Phys. B . 2020, 29(2): 028803 . **doi:** 10.1088/1674-1056/ab6655

Analysis of highly efficient perovskite solar cells with inorganic hole transport material

I Kabir, S A Mahmood

Chin. Phys. B . 2019, 28(12): 128801 . **doi:** 10.1088/1674-1056/ab520f

Insight into band alignment of Zn(O,S)/CZTSe solar cell by simulation

Zhen-Wu Jiang(姜振武), Shou-Shuai Gao(高守帅), Si-Yu Wang(王思宇), Dong-Xiao Wang(王东潇), Peng Gao(高鹏), Qiang Sun(孙强), Zhi-Qiang Zhou(周志强), Wei Liu(刘玮), Yun Sun(孙云), Yi Zhang(张毅)

Chin. Phys. B . 2019, 28(4): 048801 . **doi:** 10.1088/1674-1056/28/4/048801

Current improvement in substrate structured Sb_2S_3 solar cells with $MoSe_2$ interlayer*

Lu Liu(刘璐)[1], Sheng-Li Zhang(张生利)[1,‡], Jian-Yu Wu(吴建宇)[1], Wei-Huang Wang(王伟煌)[1], Wei Liu(刘玮)[1], Li Wu(武莉)[2], and Yi Zhang(张毅)[1,†]

[1] *Institute of Photoelectronic Thin Film Devices and Technology and Tianjin Key Laboratory of Thin Film Devices and Technology, Nankai University, Tianjin* 300350, *China*

[2] *School of Physical Science, Nankai University, Tianjin* 300071, *China*

(Received 12 March 2019; revised manuscript received 20 March 2020; accepted manuscript online 23 March 2020)

Sb_2S_3 solar cells with substrate structure usually suffer from pretty low short circuit current (J_{SC}) due to the defects and poor carrier transport. The Sb_2S_3, as a one-dimensional material, exhibits orientation-dependent carrier transport property. In this work, a thin $MoSe_2$ layer is directly synthesized on the Mo substrate followed by depositing the Sb_2S_3 thin film. The x-ray diffraction (XRD) patterns confirm that a thin $MoSe_2$ layer can improve the crystallization of the Sb_2S_3 film and induce (*hk*1) orientations, which can provide more carrier transport channels. Kelvin probe force microscopy (KPFM) results suggest that this modified Sb_2S_3 film has a benign surface with less defects and dangling bonds. The variation of the surface potential of Sb_2S_3 indicates a much more efficient carrier separation. Consequently, the power conversion efficiency (PCE) of the substrate structured Sb_2S_3 thin film solar cell is improved from 1.36% to 1.86%, which is the best efficiency of the substrate structured Sb_2S_3 thin film solar cell, and J_{SC} significantly increases to 13.6 mA/cm^2. According to the external quantum efficiency (EQE) and *C*–*V* measurements, the modified crystallization and elevated built-in electric field are the main causes.

Keywords: Sb_2S_3 thin film, super thin $MoSe_2$, built-in electric filed, Kelvin probe force microscopy

PACS: 88.40.H–, 88.40.hj **DOI:** 10.1088/1674-1056/ab8220

1. Introduction

Recently, Sb_2S_3 has received great attention for the application in solar cell. It possesses many good properties, such as a proper bandgap of ~ 1.7 eV, high light absorption coefficient ($> 10^5$ cm^{-1}), earth abundance, nontoxic source, etc.[1,2] Sb_2S_3, as a binary semiconductor compound, can keep a single phase and avoid forming the unfavorable secondary phase at high temperature,[3] which makes it a good alternative to Cu(In,Ga)Se_2 (CIGS), Cu_2ZnSnS_4 (CZTS), and CdTe absorber layers. In particular, the large bandgap provides a promising utilization for tandem dual-junction solar cells.[4]

Up to now, the highest efficient (7.5%) Sb_2S_3 solar cell is achieved by the semiconductor-sensitized device structure with glass/TCO/TiO_2/Sb_2S_3/polymer.[5] As sensitized solar cells inevitably suffer from interface degradation and device instability. To improve the device stability, much more attention is shifted to the planar structured Sb_2S_3 solar cell. A few techniques have been used to synthesize the Sb_2S_3 thin films, like chemical bath deposition,[6] solution spin coating,[7] pulse electrodeposition,[8] sputtering with post-annealing,[9] and thermal evaporation.[10] Owing to the low melting point of Sb_2S_3 (~ 550 °C), it can be synthesized at low temperatures (~ 350 °C) with good crystalline quality in a short time.[11] Hence, for the planar heterojunction Sb_2S_3 thin film solar cells, rapid thermal evaporation (RTE) is a promising approach to implement the large scale industrial preparation. At present, most of Sb_2S_3 solar cells are based on the superstrate-structured solar cell: glass/FTO/TiO_2(or CdS)/Sb_2S_3/Au. In 2016, Yuan *et al.* fabricated Sb_2S_3 thin film solar cells with large grains and preferential growth by optimizing the rapid thermal evaporation and cooling techniques, achieving a power conversion efficiency (PCE) of 3.5%.[11] As a one-dimensional ribbon material, the intra-ribbons are dominated by the covalent bonds, and the ribbons are bonded with each other by Van der Waals force. Thus, Sb_2S_3 exhibits strong anisotropy in optical and electrical properties.[12] Theoretically, most of Sb_2S_3 based devices are orientation-dependent. For this concern, Deng *et al.* successfully obtained vertical (*hk*1) orientated Sb_2S_3 by engineering TiO_2 exposure facets, which significantly improved the interface quality and intra-ribbon transport.[13] As reported previously, different substrates affect both the morphology and the crystal structure orientation of Sb_2S_3 grains.[14] The orientation of Sb_2S_3 can be tailored by modifying the substrate. The Sb_2S_3 solar cells with superstrate structure show good performances, but it is difficult to further improve the PCEs due to their

*Project supported by the National Key R&D Program of China (Grant Nos. 2019YFB1503500, 2018YFE0203400, and 2018YFB1500200), the National Natural Science Foundation of China (Grant No. U1902218), the YangFan Innovative and Entrepreneurial Research Team Project of China (Grant No. 2014YT02N037), and the 111 Project, China (Grant No. B16027).

†Corresponding author. E-mail: yizhang@nankai.edu.cn

‡Corresponding author. E-mail: shenglizhang@nankai.edu.cn

© 2020 Chinese Physical Society and IOP Publishing Ltd

simple device structures. For the purpose of thorough scientific study, substrate configuration of glass/Mo/Sb_2S_3/CdS/i-ZnO/Al-ZnO/Ni:Al is beneficial to engineer the junction interface and improve the spectral matching, which may have potential for the flexible and tandem application. In 2017, Zhang *et al.* prepared Sb_2S_3 thin film on Mo substrate by evaporating metallic Sb and then annealing in N_2/H_2S atmosphere. The best PCE of the resulting solar cells was 0.65%.[15] Later, Pan *et al.* systematically studied the effect of the substrate temperature and evaporation time on Sb_2S_3 thin films deposited by rapid thermal evaporation (RTE), and the PCE was increased up to 1.75%.[16] As mentioned in many reports, the Sb_2S_3 film suffers from the parallel orientation (*hk*0) to the substrate, especially on the Mo substrate, resulting in an unsatisfying carrier transport and large series resistance, which is detrimental for device performance.[10,11,15–18] To induce (*hk*1) preferred orientations, an extra $MoSe_2$ layer is taken into consideration. It is reported that the $MoSe_2$ possesses two-dimensional semiconductor property. Each monolayer is bonded by covalence in the order of Se–Mo–Se and all layers are stacked by weak Van der Waals interaction.[19] Wu *et al.* demonstrated that a few layers of $MoSe_2$ exhibit good electrical conductivity.[20] Thereby, a $MoSe_2$/Mo substrate is supposed to be a good alternative.

In this work, a $MoSe_2$ layer is applied to the Sb_2S_3 thin film solar cell with the substrate configuration of glass/Mo($MoSe_2$)/Sb_2S_3/CdS/iZO/AZO/Ni:Al. Systematic characterizations are employed to reveal the influence of the thin $MoSe_2$ layer on the Sb_2S_3 thin film growth and resulting solar cell. Finally, the PCE of the Sb_2S_3 thin film solar cell is increased from 1.36% to 1.86%, especially, the short circuit current J_{SC} rises from 7.11 mA/cm^2 to 13.6 mA/cm^2.

2. Experimental details

2.1. Fabrication

A two-layer structured Mo film was deposited on soda-lime glass by DC-magnetron sputtering. A pre-selenization process was carried out by chemical vapor deposition (CVD) in a quartz tube with two heating zones. The 300 mg selenium powder (99.999% purity, Alfa Aesar) and Mo substrate were located in the center of each hot zone with temperatures of 250 °C and 550 °C, respectively. The reaction was lasted for 10 min with 20 sccm Ar carrying gas flow.[20] After that, the Sb_2S_3 film was prepared by rapid thermal evaporation in a single temperature tube furnace, the substrate was maintained at 310 °C for 15 min, then rapidly rose up to 530 °C in 30 s, the evaporation duration was 100 s followed by natural cooling.[16]

Sb_2S_3 thin film solar cells were fabricated with substrate structure of glass/Mo ($MoSe_2$)/Sb_2S_3/CdS/iZO/AZO/Ni:Al. The CdS buffer layer was deposited on the Sb_2S_3 absorber by chemical bath deposition (CBD) at 75 °C for 9 min followed by sputtering 50 nm intrinsic ZnO and 500 nm ZnO:Al as the widow layer. Finally, the front electrode Ni:Al grid was prepared by electron beam evaporation, and the active area of each Sb_2S_3 solar cell was 0.18 cm^2.

2.2. Characterization

The crystal structure of the Sb_2S_3 film was characterized by x-ray diffraction (XRD) with Cu $K\alpha$ radiation source (PANalytical X'pert pro). The lattice vibration of $MoSe_2$ was analyzed by Raman spectrum at room temperature with 532 nm excitation wavelength (Horiba JobinYvon, LabRAM HR800). And the surface and cross-sectional morphologies of the Sb_2S_3 thin films were measured by scanning electric microscopy (SEM, Hitachi S-4800). The atomic force microscopy (AFM) (Dimension Icon, Bruker) was used to characterize the surface topography and thickness of the $MoSe_2$ film with an area of 5 μm^2. Kelvin probe force microscopy (KPFM) was used to detect the contact potential difference of the films, which was equipped with a Pt coated Si tip with 6 nm radius of curvature (HYDRA6R-100NG-10, APPNABQ) as the probe in a noncontact mode, and the AC voltage was adjusted by the instrument according to the films. The ultraviolet photoelectron spectroscopy (UPS; Kratos, UK) was conducted to detect the work function of the Sb_2S_3 and molybdenum electrode by using He I radiation (21.2 eV) as the excitation source. The work function of the film can be calculated by $\Phi = h\nu - (E_{\text{cutoff}} - E_{\text{F}})$. The current density–voltage (J–V) characteristics of the Sb_2S_3 thin film solar cells were measured by a solar simulator (SAN-EI XES-500T1), which was calibrated by a standard single crystal Si solar cell, under the standard AM1.5 spectrum with an illumination intensity of 1000 W/m^2 at room temperature. The capacitance–voltage (C–V) measurement was performed with a HP 4284A LCR meter in darkness at room temperature, the frequency and bias parameter were 100 KHz and 30 mV, respectively. The external quantum efficiency (EQE) of the Sb_2S_3 thin film solar cells was measured by Beijing Zolix Solar Cell Scan 100, which measured the ratio of short circuit photocurrent to incident illumination intensity in a wavelength range of 300–1300 nm.

3. Results and discussion

3.1. Growth of $MoSe_2$ and Sb_2S_3 thin films

In this work, a bare Mo substrate is exposed to the Se atmosphere for 10 min to form $MoSe_2$ first. The Ar flow is used as the carrying gas during this process. Figure 1(a) shows the Raman spectrum of this pre-selenized substrate, the peaks at 167.6 cm^{-1}, 239.2 cm^{-1}, and 286.3 cm^{-1} are attributed to E_{1g}, A_{1g}, and E_{2g} modes of the $MoSe_2$ film,

respectively.[20,21] With the help of AFM, the thickness of the $MoSe_2$ layer is measured to be about 8 nm (Fig. 1(b)). From Figs. 1(c) and 1(d), the bare Mo substrate has large grains with distinct shapes and the surface Ra (arithmetic average of absolute roughness) is 3.26 nm. For $MoSe_2$ covering on the Mo film, however, the surface Ra increases up to 4.91 nm, and grains' topography becomes much higher and steeper, which indicates that $MoSe_2$ can obviously improve the roughness of the Mo substrate and refine the surface microstructure.

Then the Sb_2S_3 absorbers are deposited on the Mo and $MoSe_2$/Mo substrates by RTE. Figure 2(a) displays the XRD patterns of the Sb_2S_3 films. All the diffraction peaks of these two thin films can be indexed to the orthorhombic Sb_2S_3 phase (space group *Pbnm*, #JCPDS 42–1393) without any impurity phase. Besides, as shown by the Raman spectrum of Sb_2S_3 on $MoSe_2$ substrate in the inset of Fig. 2(a), the peaks at 189.7 cm^{-1} and 208.3 cm^{-1} are assigned to the B_{1g} mode of S–Sb–S vibration and the peak at 251.4 cm^{-1} corresponds to the A_{1g} mode of S–Sb–S vibration, suggesting a pure phase of Sb_2S_3. Clearly, the XRD results of both samples show good crystallization, but their orientations differ due to the difference in their substrates. The Sb_2S_3 on the Mo substrate prefers (120) orientation, then moves to (310) due to the introduction of $MoSe_2$. To find out more about the variations of orientation between the Sb_2S_3 films deposited on Mo and $MoSe_2$/Mo substrates, the texture coefficient is calculated based on the following equation:[22]

$$C_{hkl} = \frac{I_{(hkl)}}{I_{0(hkl)}} \Big/ \left(\frac{1}{N} \sum_N \frac{I_{(hkl)}}{I_{0(hkl)}} \right), \tag{1}$$

where $I_{(hkl)}$ is the observed peak intensity of the (hkl) plane, $I_{0(hkl)}$ is the intensity of the standard XRD pattern, and N is the total number of counted peaks for calculation. The diffraction peaks with larger texture coefficient demonstrate better crystallization in that direction. As shown in Fig. 2(b), the Sb_2S_3 on Mo substrate presents $[hk0]$ preferred orientation, as indicated by the strong diffraction peaks of (120), (220), and (420), while the above peaks are suppressed in the Sb_2S_3 on $MoSe_2$/Mo substrate, except for the stronger (310) peak. Notably, the intensities of (221) and (211) significantly increase, which become more than twice of those for the Sb_2S_3 on Mo substrate. The calculated $(hk1)/(hk0)$ for these two samples increases from 0.18 to 0.51, which proves that the $MoSe_2$ can effectively increase the $(hk1)$ orientation. It suggests that the refined $MoSe_2$ layer with larger surface roughness could enhance $[hk1]$ orientation by providing more nucleation sites for Sb_2S_3 growth. As is well known, Sb_2S_3 exhibits a one-dimensional structure, which combines with covalent bonds along the ribbon, and the ribbons are held together by the weak Van der Waals force.[11,12] As a result, it leads to the optical property and carrier mobility being greatly anisotropic.

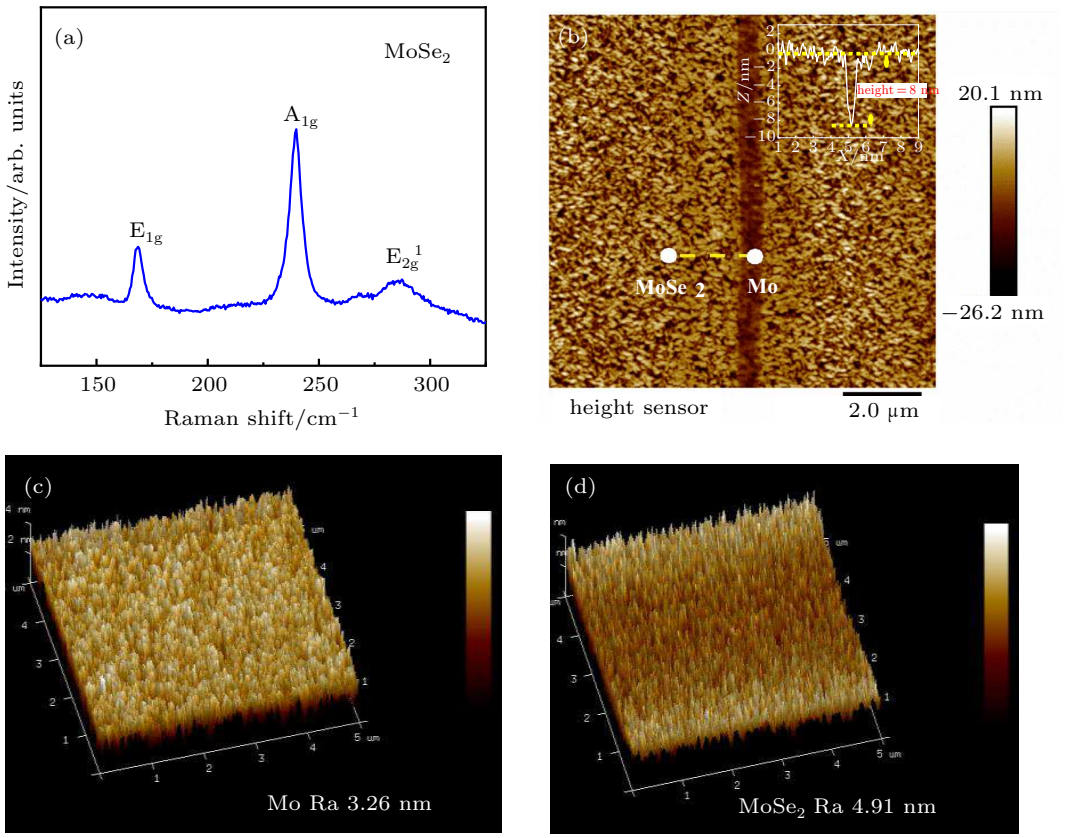


Fig. 1. (a) Raman spectrum of $MoSe_2$. (b) AFM image of $MoSe_2$ atomic layer, the inset shows $MoSe_2$ thickness of around 8 nm, and the step between Mo (dark layer in the center) and $MoSe_2$ was created by a blade. AFM images of (c) Mo surface and (d) $MoSe_2$, their surface roughnesses (Ra) are 3.26 nm and 4.91 nm, respectively.

When the films grow along (*hk*1), the ribbons will stand up or tilt on the substrate, which can offer transport tunnels to carriers. Thus, the modification of the absorber orientation would play a vital role in improving the Sb_2S_3 device performance. The Sb_2S_3 films grown on $MoSe_2$/Mo possess higher intensity of (*hk*1) than the film grown on Mo substrate, which would facilitate the transport of carriers and reduce the covalent bonds breaking at the lattice terminal.

The top view and cross-sectional SEM images of the Sb_2S_3 films deposited on Mo and $MoSe_2$/Mo substrates are shown in Figs. 2(c)–2(f). It is observed that both of them exhibit compact and continuous grains without obvious voids, but the Sb_2S_3 film on the $MoSe_2$/Mo substrate has smaller grains and some bright edges. From the cross-sectional SEM images, it can be seen that the Sb_2S_3 films are composed of large grains extending through the whole absorber, and the adhesion of the absorber to the substrate is good for these two samples.

To explore the influence of the modified Sb_2S_3 orientations on the transport of carriers, KPFM is characterized and used to detect Sb_2S_3 surface contact potential difference (CPD).[23,24] Figure 3 shows the surface topographies and CPD maps of the Sb_2S_3 thin films on different substrates from KPFM, and the line profiles reveal the relationship between the topography and CPD. From Figs. 3(c) and 3(f), we find the CPD at grain-interiors is higher than that at grain boundaries for both samples. As reported, the high potential can accumulate electrons and repel holes, the carriers can be separated by the CPD difference between grain-interior and boundaries.[25,26] For the Sb_2S_3 film on the $MoSe_2$/Mo substrate, the whole CPD is elevated, and the relative

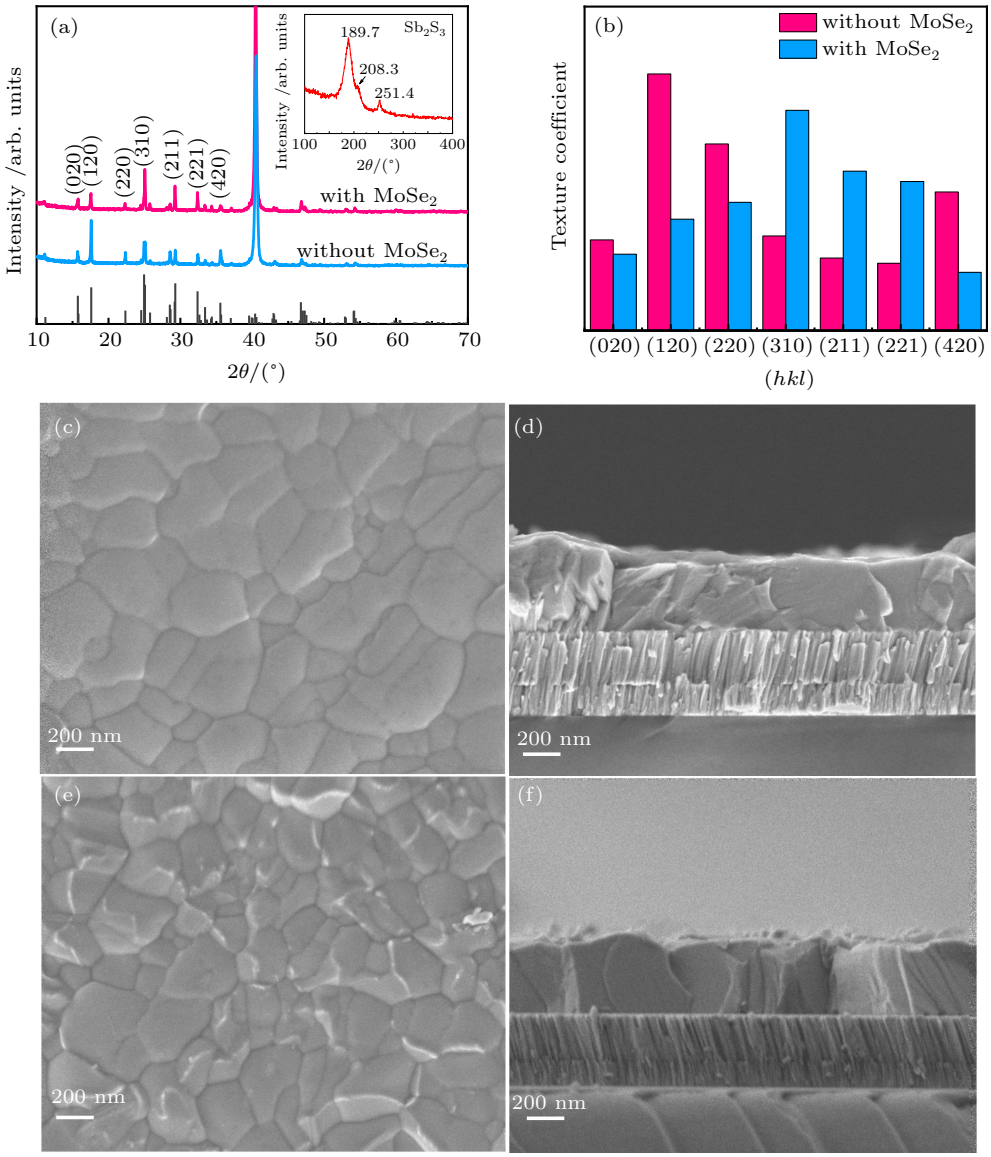


Fig. 2. (a) XRD patterns, the inset shows the Raman spectrum of Sb_2S_3 on $MoSe_2$ substrate. (b) Texture coefficients of diffraction peaks of Sb_2S_3 thin films deposited on Mo substrate with and without $MoSe_2$. SEM images: (c) top view and (d) cross section of Sb_2S_3 film deposited on Mo substrate, and (e) top view and (f) cross section of Sb_2S_3 film deposited on $MoSe_2$/Mo.

difference in CPD between peaks and dips is larger (D2>D1), revealing an enhanced capability of carrier separation, electrons and holes can effectively be collected by the corresponding electrodes.[27] The overall CPD distributions of the Sb_2S_3 films are shown in Fig. 4. Obviously, the CPD of the Sb_2S_3 film on the $MoSe_2$/Mo substrate exhibits narrower distribution than that of the Sb_2S_3 film on the bare Mo substrate. It means that the surface potential is distributed with less fluctuation,implying that the surface defects and dangling bonds decrease.[28] As discussed above, the property of the Sb_2S_3 thin film is orientation dependent, so the improvement in carrier transport can be ascribed to the increased ($hk1$) channels and less dangling bonds on the surface of Sb_2S_3 induced by the $MoSe_2$ layer.

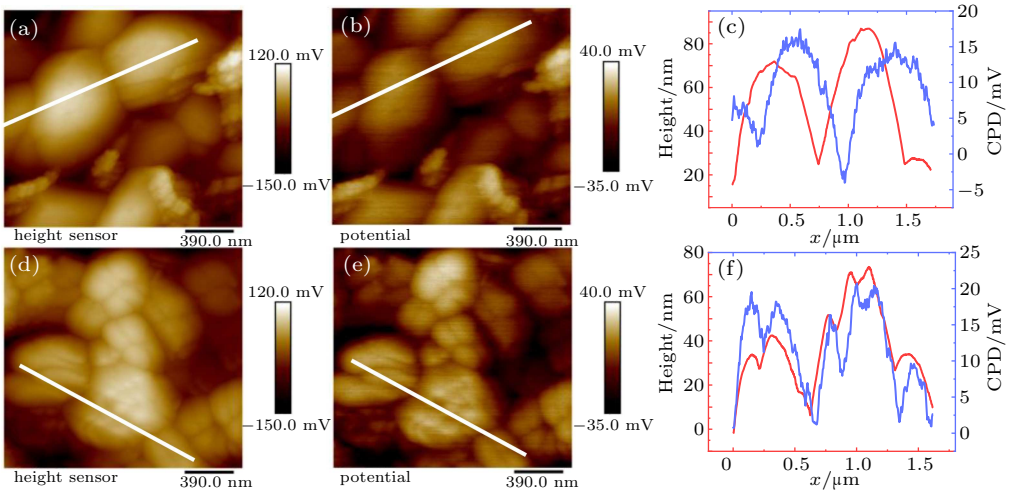


Fig. 3. (a) Surface topography, (b) CPD map, (c) topography and potential line scans for Sb_2S_3 thin film grown on Mo substrate. (d)–(e) Those for Sb_2S_3 thin film grown on $MoSe_2$ substrate. D1 and D2 in panels (c) and (f) show the difference in CPD between the peaks and dips.

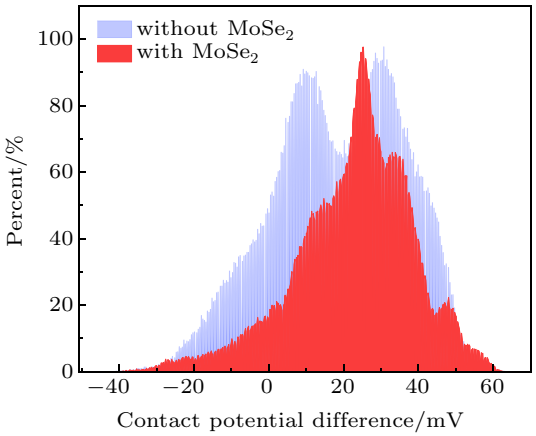


Fig. 4. Difference between surface contact potentials of Sb_2S_3 films deposited on Mo substrate with and without $MoSe_2$ derived by KPFM.

3.2. Performances of Sb_2S_3 thin film solar cells

Sb_2S_3 thin film solar cells are fabricated with substrate configuration of glass/Mo ($MoSe_2$)/Sb_2S_3/CdS/iZO/AZO/Ni:Al. The device parameter distributions in Figs. 5(a)–5(d) reveal a total improvement of J_{SC} from 8.32 mA/cm^2 to 12.48 mA/cm^2 on average. As for the open circuit voltage (V_{OC}) and fill factor (FF), they are nearly the same. As a result, the efficiency is increased from 1.27% to 1.62% on average. Figure 5(e) displays the best J–V curves of the optimal Sb_2S_3 solar cells deposited on the Mo substrate and the $MoSe_2$/Mo substrate. The best device parameters are summarized in Table 1. It is observed that the PCE of the Sb_2S_3 solar cells is improved from 1.36% to 1.86% by inserting a thin $MoSe_2$ layer between the Sb_2S_3 layer and Mo layer. For the Sb_2S_3 solar cell with the $MoSe_2$ interlayer, J_{SC} dramatically increases from 7.11 mA/cm^2 to 13.6 mA/cm^2, though V_{OC} declines from 490 mV to 466 mV and FF presents a slight drop. Considering the high work function of $MoSe_2$, the band structure at back contact was first used to account for the improved J_{SC}, but the work functions of the Sb_2S_3 film and Mo film measured by UPS show little difference. Specifically, their work functions are 4.27 eV and 4.86 eV, respectively (Fig. 6). Thus Sb_2S_3/Mo can naturally form ohmic contact, this means that a super thin $MoSe_2$ has no influence on the rear band alignment. After that, we find that the enhancement of J_{SC} can be explained by EQE in Fig. 5(f). A considerable improvement of quantum yield in the long wavelength range (550–750 nm) can be seen and the peak EQE is over 70%, higher than that of the device reported in the literature. Besides, the limit of light absorption in long wavelength broadens to ca. 800 nm. As is well known, the increase in long wavelength reveals a correlation between the absorber crystallization and the back-interface modification. From this point, we conclude that the $MoSe_2$ interlayer can not only modify the crystallization of Sb_2S_3 with ($hk1$) orientation but also serve as the texture of light trapping. In addition, a small amout of Se is supposed to diffuse into Sb_2S_3 during the heating process, because the band gap decreases from 1.73 eV to 1.65 eV (see the inset in Fig. 5(f)). As reported previously, sulfur vacancy (V_S) is a deep-donor defect, which usually

forms during Sb_2S_3 deposition at high temperature.[12] But V_S can be easily replaced by Se, which helps to passivate the deep defects and improve the carrier density.[29] Considering the possibility of amorphous Se being absorbed on the $MoSe_2$ surface, we speculate that some deep defects of Sb_2S_3 may be passivated by Se diffusion.

Table 1. Device performance parameters of Sb_2S_3 thin film solar cells.

	V_{OC}/mV	J_{SC}/mA·cm^{-2}	FF/%	PCE/%
Without $MoSe_2$	490	7.11	32.4	1.36
With $MoSe_2$	466	13.6	31.06	1.86

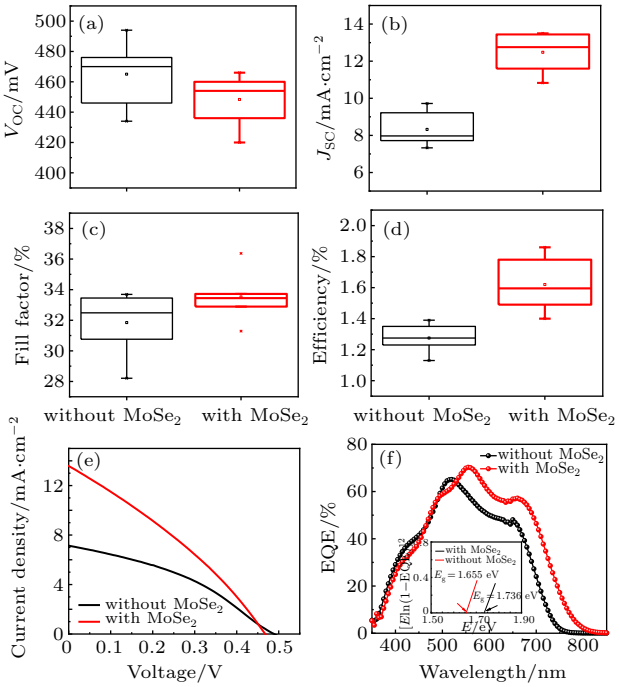


Fig. 5. Distributions of device parameters (a) V_{OC}, (b) J_{SC}, (c) fill factor, and (d) efficiency. (e) The J–V curves and (f) EQE spectra of optimal Sb_2S_3 solar cells deposited on Mo substrate with and without $MoSe_2$, the inset shows the band gap extracted from the EQE data.

The C–V measurement is employed to get further insight into the J_{SC} enhancement. The abrupt p–n$^+$ heterojunction can be viewed as a parallel-plate capacitor model. We can obtain the carrier concentration, depletion width, and built-in potential (V_{bi}) from the following equations:[29,30]

$$N_{A,p} = \frac{-2N_{D,n}\varepsilon_{r,n}}{\frac{d(1/c^2)}{dV}qN_{D,n}\varepsilon_{r,p}\varepsilon_{r,n}A^2\varepsilon_0 + 2\varepsilon_{r,p}}, \quad (2)$$

$$\frac{1}{c^2} = \frac{2(V_{bi}-V)}{qA^2\varepsilon_0\varepsilon_{r,p}N_{A,p}}, \quad (3)$$

$$W_d = \frac{\varepsilon_0\varepsilon_r A}{C}, \quad (4)$$

where $N_{A,p}$, V, V_{bi}, q, ε_0, ε_r, W_d, and A represent the carrier concentration in the Sb_2S_3 thin film, bias voltage, built-in potential, elementary charge, vacuum permittivity, relative permittivity, depletion width, and device area, respectively. The C–V and $1/C^2$–V curves of the Sb_2S_3 thin film solar cells without and with a $MoSe_2$ are plotted in Fig. 7. It is observed that the capacity increases with bias voltage increasing. As the depletion width decreases, the capacity gradually turns into a constant. The built-in voltage V_{bi} can be estimated by the x-intercept in the $1/C^2$–V plot and $E_{in} = V_{bi}/W_d$ is used to calculate the built-in electric field (E_{in}).[31,32] The values of V_{bi}, W_d, $N_{A,p}$, and E_{in} are summarized in Table 2.

Table 2. Summary of built-in potential V_{bi}, depletion width W_d, carrier density $N_{A,p}$, and built-in electric field V_{bi}.

	V_{bi}/mV	W_d/nm	$N_{A,p}$/cm^{-3}	E_{in}/V·cm^{-1}
Without $MoSe_2$	347	858	8.12×10^{15}	4×10^3
With $MoSe_2$	538	647	1.8×10^{16}	8.3×10^3

Compared with the Sb_2S_3 solar cell without $MoSe_2$, the sample with $MoSe_2$ shows short W_d (647 nm) and great carrier density (1.8×10^{16} cm^{-3}). Furthermore, the E_{in} of this device is almost twice as large as that of the sample reported in the literature. The large E_{in} will facilitate the carrier separation, which is consistent with the result of KPFM, thus contributes to an enhanced J_{SC}. We also note that the built-in potential of the Sb_2S_3 solar cell with $MoSe_2$ is 538 mV, which is higher than 347 mV of the control-one, but the V_{OC} improvement is not notable, which is considered to be neutralized by the decreased band gap.

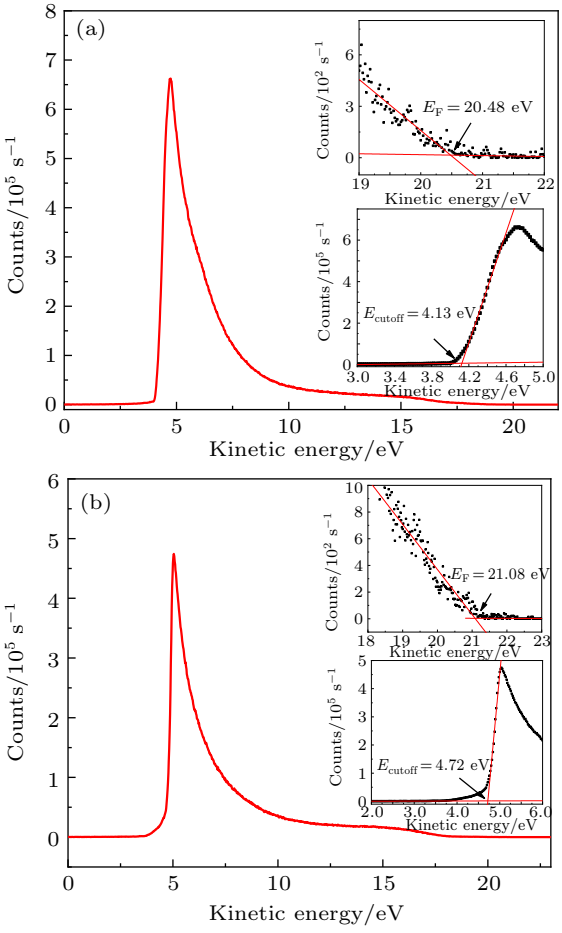


Fig. 6. UPS of (a) Sb_2S_3 film and (b) Mo film, showing the work functions of Sb_2S_3 and Mo being 4.27 eV and 4.86 eV, respectively. (a) $\Phi Sb_2S_2 = E_{hv} - (E_F - E_{cutoff}) = 21.22 - (21.08 - 4.13) = 4.27$ eV. (b) $\Phi Mo = E_{hv} - (E_F - E_{cutoff}) = 21.22 - (21.08 - 4.72) = 4.86$ eV.

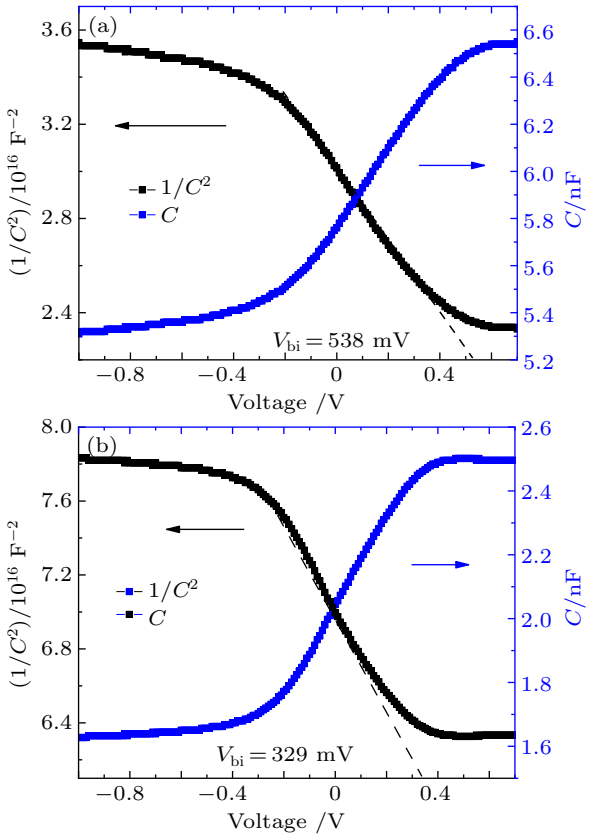


Fig. 7. The C–V and $1/C^2$–V curves for Sb_2S_3 solar cells (a) without and (b) with $MoSe_2$.

4. Conclusions

We fabricate Sb_2S_3 thin film solar cells with substrate configuration of glass/Mo ($MoSe_2$)/Sb_2S_3/CdS/iZO/AZO/Ni:Al grid. A thin $MoSe_2$ layer is developed before the deposition of the Sb_2S_3 thin film. The schematical investigation indicates that a thin $MoSe_2$ layer with refined micro-structure can increase the ($hk1$) orientation of Sb_2S_3, providing more carrier transport channels. The concentrated CPD distribution from KPFM suggests less interface defects and dangling bonds on the surface of Sb_2S_3 on the $MoSe_2$/Mo substrate. What is more, the CPD variations in both samples confirm an improvement of electrons barrier at GBs, which will facilitate the carrier separation. Consequently, the PCE of the Sb_2S_3 solar cell is improved from 1.36% to 1.86% by inserting the $MoSe_2$ layer between the Sb_2S_3 laye layer and the Mo layer. The J_{SC} dramatically increases from 7.11 mA/cm^2 to 13.6 mA/cm^2. EQE and C–V measurements further disclose the role of $MoSe_2$ in enhancing J_{SC} for this optimal device. The $MoSe_2$ can not only improve the crystallization of Sb_2S_3 with ($hk1$) orientation, but also serve as a light tapping texture. Moreover, a small amount of Se is supposed to diffuse into Sb_2S_3 during the heating process, which is considered to passivate the deep defects and promote the device performance.

Acknowledgements

We thank Prof. Y. Sun and Prof. J. Ao for helpful discussion. We also thank Dr. F. Liu for XRD measurement.

References

[1] Ghosh C and Varma B P 1979 *Thin Solid Films* **60** 61
[2] Moon S J, Itzhaik Y, Yum J H, Zakeeruddin S M, Hodes G and Grätzel M 2010 *J. Phys. Chem. Lett.* **1** 1524
[3] Kondrotas R, Chen C and Tang J 2018 *Joule* **2** 857
[4] Yu Z, Leilaeioun M and Holman Z 2016 *Nat. Energy* **1** 16137
[5] Choi Y C, Lee D U, Noh J, Kim E and Im S H 2014 *Adv. Funct. Mater.* **24** 3587
[6] Shaji S, Garcia L V, Loredo S L, Krishnan B, Aguilar-Martinez J A, Das Roy T K and Avellaneda D A 2017 *Appl. Surf. Sci.* **393** 369
[7] Sung S J, Gil E K, Lee S J, Choi Y C, Yang K J, Kang J K, Cho K Y and Kim D H 2017 *J. Ind. Eng. Chem.* **56** 196
[8] Avilez-Garcia R G, Meza-Avendaño C A, Pal M, Paraguay-Delgado F and Mathews N R 2016 *Mater. Sci. Semicond. Process.* **44** 91
[9] Medina-Montes M I, Montiel-González Z, Mathews N R and Mathew X 2017 *J. Phys. Chem. Solids* **111** 182
[10] Escorcia-García J, Becerra D, Nair M T S and Nair P K 2014 *Thin Solid Films* **569** 28
[11] Yuan S, Deng H, Dong D, Yang X, Qiao K, Hu C, Song H, Song H, He Z and Tang J 2016 *Energy Mater. Sol. Cells* **157** 887
[12] Tumelero M A, Faccio R and Pasa A A 2016 *J. Phys. Chem. C* **120** 1390
[13] Deng H, Zeng Y, Ishaq M, Yuan S, Zhang H, Yang X, Hou M, Farooq U, Huang J, Sun K, Webster R, Wu H, Chen Z, Yi F, Song H, Hao X and Tang J 2019 *Adv. Funct. Mater.* **29** 1901720
[14] Kondrotas R, Zhang J, Wang C and Tang J 2019 *Sol. Energy Mater. Sol. Cells* **199** 16
[15] Zhang L, Zhuang D, Zhao M, Gong Q, Guo L, Ouyang L, Rujun S, Yaowei W, Lyu X and Peng X 2017 *Mater. Lett.* **208** 58
[16] Pan G, Wang D, Gao S, Gao P, Sun Q, Liu X, Zhou Z, Sun Y and Zhang Y 2019 *Sol. Energy* **182** 64
[17] Ito S, Tsujimoto K, Nguyen D C, Manabe K and Nishino H 2013 *Int. J. Hydrogen Energy* **38** 16749
[18] Wang X, Li J, liu w, Yang S, Zhu C and Chen T 2017 *Nanoscale* **9** 3386
[19] Xia J, Huang X, Liu L Z, Wang M, Wang L, Huang B, Zhu D D, Li J J, Gu C Z and Meng X M 2014 *Nanoscale* **6** 8949
[20] Wu Z, Tai G, Wang X, Hu T, Wang R and Guo W 2018 *Nanotechnology* **29** 125605
[21] Soubelet P, Bruchhausen A, Fainstein A, Nogajewski K and Faugeras C 2016 *Phys. Rev. B* **93** 155407
[22] Li Z, Chen X, Zhu H, Chen J, Guo Y, Zhang C, Zhang W, Niu X and Mai Y 2017 *Sol. Energy Mater. Sol. Cells* **161** 190
[23] Chen Y J, Zhang M J, Yuan S, Qiu Y, Wang X B, Jiang X, Gao Z, Lin Y and Pan F 2017 *Nano Energy* **36** 303
[24] Vishwakarma M, Varandani D, Andres C, Romanyuk Y E, Haass S G, Tiwari A N and Mehta B R 2018 *Sol. Energy Mater. Sol. Cells* **183** 34
[25] Zhao X, Kou D, Zhou W, Zhou Z, Meng Y, Meng Q, Zheng Z and Wu S 2019 *J. Mater. Chem. A* **7** 3135
[26] Xin H, Vorpahl S, Collord A, Braly I, Uhl A, Krueger B, Ginger D and Hillhouse H 2015 *Phys. Chemistry Chemical Physics : PCCP* **17** 23859
[27] Yun J S, Seidel J, Kim J, Soufiani A M, Huang S, Lau J, Jeon N J, Seok S I, Green M A and Ho B 2016 *Adv. Energy Mater.* **6** 1600330
[28] Park J, Huang J, Yun J, Liu F, Ouyang Z, Sun H, Yan C, Sun K, Kim K, Seidel J, Chen S, Green M A and Hao X 2018 *Adv. Energy Mater.* **8** 1701940
[29] Yuan S, Deng H, Yang X, Hu C, Khan J, Ye W, Tang J and Song H 2017 *ACS Photon.* **4** 2862
[30] Deng H, Yuan S, Yang X, Cai F, Hu C, Qiao K, Zhang J, Tang J, Song H and He Z 2017 *Mater. Today Energy* **3** 15
[31] Zeng Y, Zhang S, Li X, Ao J, Sun Y, Liu W, Liu F, Gao P and Zhang Y 2019 *Chin. Phys. B* **28** 058101
[32] Zhang Y, Li B, Dang X, Wu L, Jin J, Li F, Ao J and Sun Y 2011 *Chin. Phys. B* **20** 116802